


KIC 4473933: A Magnetically Active Long Period System

Ezgi Yoldaş^{*} 

Ege University, Science Faculty, Department of Astronomy and Space Sciences, 35100 Bornova, İzmir, Turkey.

Accepted December 17, 2021. Revised June 20, 2021. Received May 8, 2021.

Abstract

Taking into account the results found by analyzing the Kepler data together with our new photometric observations as well as new spectroscopic observations, we present new findings about a highly eccentric detached eclipsing binary, KIC 4473933. For the primary and secondary components, we estimated that the radii of components were $0.98 R_{\odot}$ and $8.90 R_{\odot}$, while the masses were $0.36 M_{\odot}$ and $0.74 M_{\odot}$. Examining the ASAS data, we realized that the variation out-of-eclipses was due to cold stellar spots. When this data was phased according to the rotational period of 67.575786 d given in the literature, we detected two spot areas on the surface of the active component that exhibited 87.719 d and 94.340 d longitudinal migration movements.

Key words: techniques: photometric – methods: data analysis – methods: statistical – binaries: eclipsing – stars: KIC 4473933

1 Introduction

In the beginning, the main aim of Kepler Mission is to discover the exo-planets (Borucki et al. 2010; Koch et al. 2010; Caldwell et al. 2010). To achieve this aim, an instruments like the Kepler Satellite, with high quality and precision are required for the photometric observations. Indeed, the high-quality data obtained from Kepler Mission reveal the existence of numerous exo-planets as well as the large number of variable stars, such as some new eclipsing binaries (Slawson et al. 2011; Matijević et al. 2012).

Most of these discovered eclipsing binaries have chromospherically active components, and these systems are generally known as BY Dra and RS CVn binaries (Kunkel 1975; Rodono 1986). These systems exhibit the magnetic activity, such as stellar spot activity. In these systems, both components at least one of them must be a main sequence star, while both stars are of late spectral type. In the literature, Kron (1952) found some sinusoidal variations at out-of-eclipses of the eclipsing binary star YY Gem. This variation was explained as a heterogeneous temperature on active component's surface. Kunkel (1975) called this type stars as BY Dra variable. RS Cvn type stars exhibit the same variability as BY Dra stars. Despite the BY Dra variable, one component in the RS CVn systems is evolved star and it is generally a giant or subgiant star (Thomas & Weiss 2008). Sixty-five percent of the stars in our Galaxy are late type stars, and seventy-five percent of them show magnetic activity (Rodono 1986). López-Morales (2007) and Morales et al. (2008, 2010) demonstrate that magnetic activity dramatically affects stellar structure and also their evolutions.

In this paper, KIC 4473933 is examined for its possible pulsations. The orbital period of KIC 4473933 is given as 103.5926245 days (Slawson et al. 2011). Tayar et al. (2015) reported the temperature of the system as 4493.6 K with $\log(g) = 3.08 \text{ cm s}^{-2}$, $[\text{Fe}/\text{H}] = -0.167$, $v \sin i = 13.6 \text{ km/s}$, while Mathur et al. (2017) gave the temperature of the system as 4505 K with $\log(g) = 4.644 \text{ cm s}^{-2}$, $[\text{Fe}/\text{H}] = -0.28$. In the same study, the radius and mass are given as $R = 0.633 R_{\odot}$ and $M = 0.644 M_{\odot}$. The most recent study of KIC 4473933

is by Benbakoura et al. (2021). They analysed system's several spectra together with its Kepler photometric data. They obtained system's radial velocity variation, and they exhibited that the target is a single-line spectroscopic binary (SB1), while they found remarkable Ca II H&K emission. Modelling the light curve with JKTEBOP, Benbakoura et al. (2021) found that the ratio of radii is 0.118 ± 0.002 , and the inclination (i) is $84^{\circ}27' \pm 0^{\circ}009'$, and they determined the ratio of L_1/L_2 as 0.0874 ± 0.0002 . In the light curve analysis, the argument of periastron w was found to be 210 ± 4 , while the eccentricity (e) was found to be 0.279 ± 9 . Depending on the target's spectra, Benbakoura et al. (2021) determined the temperature of the primary component as $4530 \pm 220 \text{ K}$, and they estimated $7172 \pm 344 \text{ K}$ for the secondary component. The most interesting result they found is that the rotational period of the target was found to be $68.4 \pm 6.1 \text{ d}$. This means that the components do not rotate synchronously.

In this study, we try to reveal the nature of the target, analyzing variation detected in the light curve. In the next sections, we summarize the analyzed data. The new observations are described in §2.1. The O-C variation analysis are given in §2.2. We describe the light curve model of the target in §2.3, while we tried to described the problematic nature of KIC 4473933 with new data and observations in §2.4. We summarize and discuss our findings in the last section.

2 Data and Analysis

The large part of data analyzed in this study were taken from the Kepler Eclipsing Binary Catalog (Kirk et al. 2016), where the data are available for numerous targets (Borucki et al. 2010; Koch et al. 2010; Caldwell et al. 2010; Slawson et al. 2011; Matijević et al. 2012). The data obtained in this mission have the highest quality and sensitivity ever reached in the astronomical photometry (Jenkins et al. 2010a,b). For the analysis and model, we used the data shown in Fig. 1 (Slawson et al. 2011; Matijević et al. 2012). We used the long cadence data given from Quarter 0 to 17, apart from Quarters 4, 6, 10, 14. We used the short cadence data given in Quarter 4.

* ezgiyoldas@gmail.com

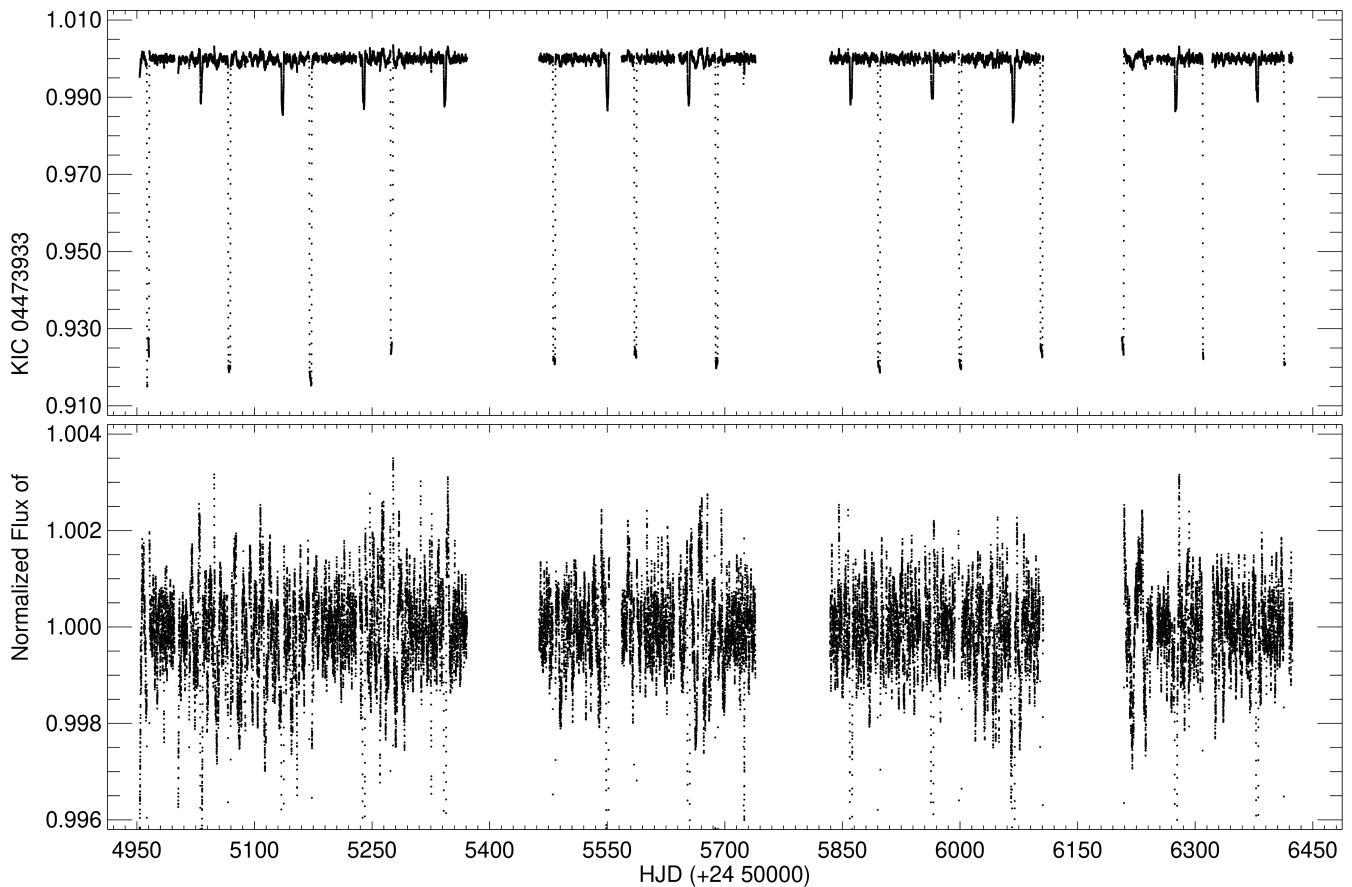


Figure 1. KIC 4473933's light curve of the target obtained from the detrended long-cadence data taken from the Kepler Mission database are shown. Whole the light curve was plotted in the upper panel, while the light variation at out-of-eclipses was plotted to permit a better view in the bottom panel of the figure.

2.1 New Observations

In this study, we observed with a ground-based telescope to obtain a minimum time. KIC 4473933 was listed as $12^{\text{m}}10$ of V band in the Tycho Input Catalog (Egret et al. 1992), while the B, V, R, J, H and K magnitudes were also listed as $13^{\text{m}}10$, $12^{\text{m}}46$, $11^{\text{m}}40$, $9^{\text{m}}853$, $9^{\text{m}}237$, $9^{\text{m}}097$ in the NOMAD Catalog, respectively (Zacharias et al. 2004). The B–V color index was tabulated as $1^{\text{m}}029$ by Henden et al. (2015).

We observed the target with a thermoelectrically cooled ALTA Apogee U42 2048×2048 pixel CCD camera attached to a 40-cm Schmidt-Cassegrain-type MEADE telescope at the Ege University Observatory (EUO). Observations were made in clear band during 4 nights on 2018 September 19, 20, 21 and 22 for KIC 4473933. KIC 4570372 was chosen as a comparison star, while KIC 4571226 was chosen as a check star. Although the target and comparison stars are very close on the sky, using the calibration described by Hardie (1964), the differential atmospheric extinction corrections were applied. Atmospheric extinction coefficients were obtained from observations of the comparison stars on each night. Heliocentric corrections were also applied to the times of the observations. The mean averages of the standard deviations vary from $0^{\text{m}}007$ to $0^{\text{m}}009$ for observations acquired in the clear band. To compute the standard deviations of observations, we used the standard deviations of the reduced differential magnitudes in the sense of

Table 1. Observations obtained at Ege University Observatory. Here, the first 5 lines are tabulated for the target. The rest of them are given in online archive.

HJD	Δm (mag in clear band)
2458381.2108145	-0.799
2458381.2115437	-0.798
2458381.2122729	-0.787
2458381.2129905	-0.790
2458381.2137196	-0.790

comparison minus check stars for each night. No variation was observed in the brightness of comparison stars. All the observations have been tabulated in Table 1. Just a portion of the whole table is listed in the paper, whole table is given in entire database of the journal.

In addition to the photometric observations, we recorded a spectrum with the signal-to-noise ratio (hereafter SNR) between 50 and 100 depending on atmospheric conditions on KIC 4473933 on August 31, 2019 (HJD 2458727.32793), when it is corresponding to the 0.326 phases of the light curve. We carried out spectroscopic observation of the target with 1.5-m Russian-Turkish telescope and Turkish Faint Object Spectro-

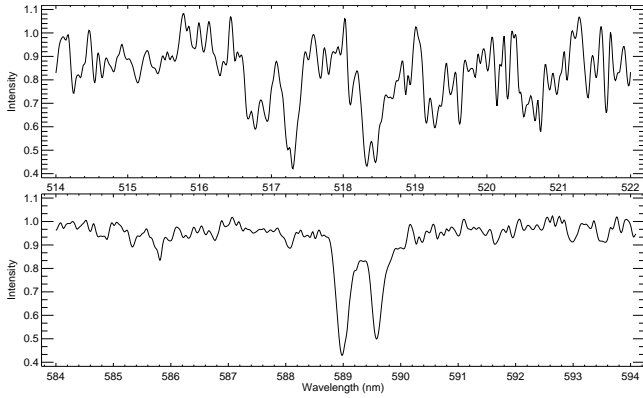


Figure 2. The line profiles of Mg I b ($\lambda 516.7$ nm, $\lambda 517.3$ nm, $\lambda 518.4$ nm) triplets and Na I D1 ($\lambda 589.6$ nm), D2 ($\lambda 589.0$ nm) obtained from KIC 4473933 are shown.

graph Camera (TFOSC) at TÜBİTAK National Observatory. Using the échelle mode of the TFOSC, we achieve actual resolution of $R = \lambda/\Delta\lambda \sim 3000$ around 5500 \AA . Whole spectrum covers wavelength interval between $3900\text{--}9100 \text{ \AA}$ in 11 échelle orders. All spectra were recorded with back illuminated 2048×2048 pixels CCD camera, which has pixel size of $15 \times 15 \mu\text{m}^2$. In addition to observing the target star, we also observed ι Psc (HD 222368, F7V, $v_r = 5.656 \text{ km/s}$; Gray et al. 2001) to determine spectral type of the target star, whose spectra were also used as the radial velocity template.

Recorded raw spectra were reduced by following conventional échelle reduction steps, starting by bias correction to all images and followed by obtaining bias corrected normalized flat field image from halogen lamp frames, dividing all science and Fe-Ar calibration images by normalized flat field image, scattered light correction to bias and flat field corrected science images. After these main reduction steps, reduced raw spectra were extracted from images and wavelength calibration was applied to the science images. In the final steps, wavelength calibrated the science images were normalized to the unity by using cubic spline functions. All of these steps were applied under IRAF¹ environment. As an example of the data obtained from spectral observation, the spectrum in the range of $514\text{--}522 \text{ nm}$ and $584\text{--}594 \text{ nm}$ and the lines in these regions known to be sensitive to stellar activity are shown in Fig. 2.

The first step of our analysis is to determine the radial velocities of the components and spectroscopic orbit of the system. We cross-correlate the observed spectrum of KIC 4473933 with spectra of template star ι Psc, as described in Tonry & Davis (1979). In practice we use `fxcor` task in IRAF environment. We obtain acceptable cross-correlation signal for just one component in échelle orders 5 and 6, which cover wavelength range between $4900\text{--}5700 \text{ \AA}$. The obtained radial velocity is plotted in Fig. 3 as a red filled circle.

We use high SNR spectra of 54 Psc (K0V) (Gray et al. 2003), HD 190404 (K1V) (Frasca et al. 2009) and τ Cet (G8.5V) (Gray et al. 2006) as comparison templates to estimate the spectral type of the observable component. Spectral

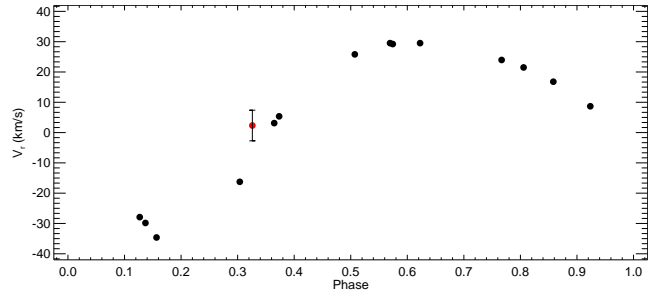


Figure 3. Observed radial velocity variation obtained from KIC 4473933. In the figure, the filled black circles were obtained by Benbakoura et al. (2021), while the filled red circle is obtained in this study.

types of these stars were reliably determined via high resolution spectroscopic observations in the given references. We calculate composite spectrum for each binary combination of template stars, (54 Psc+HD 190404, HD 190404+ τ Cet, HD 190404+HD 190404, etc.) and compare each calculated composite spectrum with the observed spectrum of KIC 4473933. For a given binary combination, we first apply proper radial velocity shift to the spectrum of each template star to match their spectral lines to the lines of corresponding component along the wavelength. Then, we calculate resulting composite spectrum by considering the luminosity ratio of the components that we find from light curve modelling. We iterate this process until we achieve agreement between spectral types, and luminosity ratio found from light curve modelling. However we could not achieve no model to fitted observed spectrum. Then, we used several synthetic templates derived for different effective temperatures and metallicity values to determine the spectral type of the target. Taking the list of spectral lines between 300 and 1100 nm from Vienna Atomic Line Database (VALD, Ryabchikova et al. 2015), the synthetic templates were derived with the `iSpec` software (Blanco-Cuaresma et al. 2014) by using `Spectrum` code (Gray & Corbally 1994) depending on the ATLAS9 model atmospheres derived by Castelli & Kurucz (2004). Comparing each spectrum of target to all the synthetic templates, we determined the spectral type of target. In a results, we determined the temperature of the target as $4500 \pm 200 \text{ K}$.

2.2 Orbital Period Variation

To obtain the light curves with adjusted minima, we firstly determined the minima times of the target to adjust the minima times. The minima times were computed with a script depending on the method described by Kwee & van Woerden (1956). In this method, taking symmetrically increasing and decreasing parts of minima, the minima times were computed by using a polynomial function. Secondly, we calculated the differences between observed and computed the minima times. For this aim, we used the light elements taken as the initial values from the Kepler Eclipsing Binary Catalog given by Eq. 1.

$$\text{BJD (Hel.)} = 24\,54965.00543 + 103^{\text{d}}59815 \times E \quad (1)$$

After calculating the $(O-C)_I$ differences, we applied a linear correction to the computed residuals, to obtain the $(O-C)_{II}$ differences. Here, we must noted that we applied the linear corrections with different coefficients for the primary and secondary minima times, because of the target having eccentric

¹ The Image Reduction and Analysis Facility is hosted by the National Optical Astronomy Observatories in Tucson, Arizona at <http://ast.noao.edu/>

Table 2. The minima times of target and $(O-C)_I$ and $(O-C)_{II}$ residuals obtained from the Kepler LC data. In the table, the minimum time for 19 of epoch was computed from the EUO observations.

HJD (+24 00000)	Epoch	Type	$(O-C)_I$ (day)	$(O-C)_{II}$ (day)
54964.33831 ± 0.01787	0	I	-0.66712 ± 0.10112	0.02363 ± 0.10018
55067.86617 ± 0.01787	1	I	-0.73741 ± 0.10112	-0.05124 ± 0.10018
55171.51638 ± 0.01787	2	I	-0.68535 ± 0.10112	-0.00377 ± 0.10018
55482.45928 ± 0.01787	5	I	-0.53689 ± 0.10112	0.13094 ± 0.10018
55585.90110 ± 0.01787	6	I	-0.69323 ± 0.10112	-0.02998 ± 0.10018
55689.48548 ± 0.01787	7	I	-0.70700 ± 0.10112	-0.04833 ± 0.10018
55896.70927 ± 0.01787	9	I	-0.67950 ± 0.10112	-0.03000 ± 0.10018
56000.33104 ± 0.01787	10	I	-0.65588 ± 0.10112	-0.01097 ± 0.10018
56103.96060 ± 0.01787	11	I	-0.62447 ± 0.10112	0.01586 ± 0.10018
58383.20874 ± 0.01787	33	I	-0.53561 ± 0.10112	0.00387 ± 0.10018
55136.00291 ± 0.02710	1.5	II	15.60026 ± 0.08666	0.11099 ± 0.07621
55239.40470 ± 0.02710	2.5	II	15.40390 ± 0.08666	-0.06562 ± 0.07621
55342.89171 ± 0.02710	3.5	II	15.29276 ± 0.08666	-0.15700 ± 0.07621
55550.40327 ± 0.02710	5.5	II	15.60802 ± 0.08666	0.19779 ± 0.07621
55653.74726 ± 0.02710	6.5	II	15.35386 ± 0.08666	-0.03661 ± 0.07621
55860.66455 ± 0.02710	8.5	II	15.07486 ± 0.08666	-0.27609 ± 0.07621
55964.80395 ± 0.02710	9.5	II	15.61611 ± 0.08666	0.28492 ± 0.07621
56068.06391 ± 0.02710	10.5	II	15.27791 ± 0.08666	-0.03351 ± 0.07621
56275.22931 ± 0.02710	12.5	II	15.24702 ± 0.08666	-0.02488 ± 0.07621

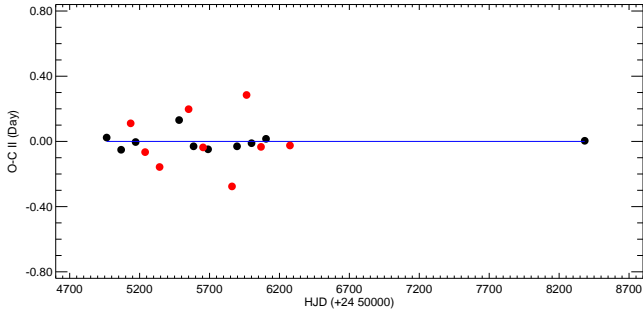


Figure 4. The variations of the $(O-C)_{II}$ residuals for the target. In the figure, the filled black circles represent the minima times of the primary minima, while the filled red circles represent the minima times of the secondary minima. The result obtained by applying the linear corrections to the primary and secondary minima separately are shown. In addition, the derived best-linear fit is represented with the smooth blue line.

orbits. In the analysis, we first applied the linear corrections to both the primary and secondary minima together. However, we have noticed that the linear corrections do not work correctly. Then, we have applied the linear corrections to the primary and secondary minima separately. In this point, we obtained the adjusted light elements given with Eq. 2 for the primary minima times, while we reached the adjusted light elements given with Eq. 3 for the secondary minima times.

$$\text{BJD (Hel.)} = 24\ 54964.31468(2) + 103^{\text{d}}60273(4) \times E \quad (2)$$

$$\text{BJD (Hel.)} = 24\ 54980.52343(6) + 103^{\text{d}}57838(4) \times E \quad (3)$$

All the results are tabulated in Table 2. In the table, the observed minima times are listed in the first column, the epoch number and the minima types are listed in the next columns. Calculated $(O-C)_I$ and derived $(O-C)_{II}$ residuals are in the last two column, respectively. The variations of the $(O-C)_{II}$ residuals are shown in Fig. 4.

2.3 Light Curve Analysis

The light curve of target was analyzed by using the PyWD2015 software (Güzel & Özdarcan 2020), which is a new GUI software developed for the 2015 version of the Wilson Devinney Code (Wilson & Devinney 1971; Wilson & Van Hamme 2014), to compute the physical parameters of each component. In the analysis, the averaged data computed phase by phase with interval of 0.001 were used to discard the scattering. The PyWD2015 needs the temperature value for the primary component in the analysis. In the literature, there are lots of temperature estimations for the system. However, the most recent adjusted temperature value is given in the MAST Database, where the temperature is given as 4575 K.

A light curve solution was found by Benbakoura et al. (2021) for the first time in the literature. They analysed the light curve by the JKTEBOP software under some assumptions. As it can be seen from the paper, they found the temperature of the primary component as 4530 K from the spectroscopy. Taking into count the ratio of the luminosities obtained from the JKTEBOP analyses, they also determined the ratio of the temperatures (T_2/T_1) as 1.5828. Considering this ratio with the primary component's temperature, they found the secondary component's temperature as 7172 K.

In the first step, we tried the analyse the light curve with the parameters given by Benbakoura et al. (2021). However, the PyWD2015 software does not give any solution. The analyses persistently adjusted the temperature of the secondary component toward 3500 K. Then, we tried to analyse the light curve using by the JKTEBOP software with the parameters of Benbakoura et al. (2021). We saw that it needs to take the mass ratio (q) as -1, which means that the JKTEBOP software modelled the light curve taking the components as two circles in the different radii, not the spheres. For this reason we tried to analyse the light curve under three different assumptions in order to obtain an astrophysically acceptable solution.

First of all, we fixed the temperature of the primary component given in the MAST Database, while the temperature

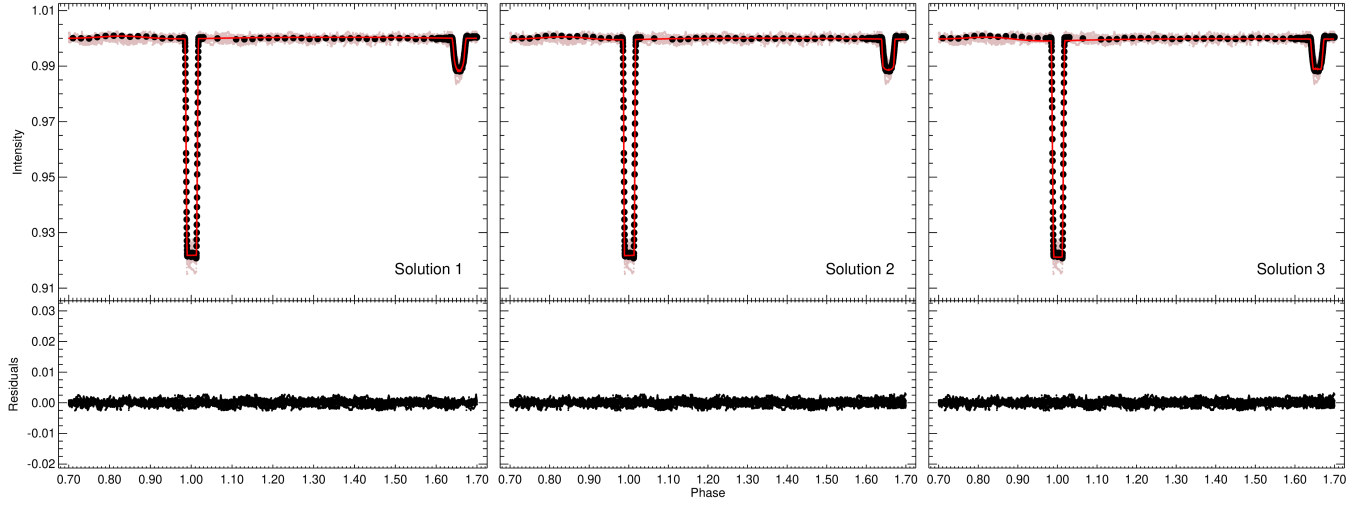


Figure 5. The light curve and its synthetic models derived by the PyWD2015 software (Güzel & Özdarcan 2020) for different assumptions. The synthetic curves are obtained from the Solutions 1, 2 and 3 from the left panel to the right.

of the secondary component was taken as an adjustable free parameter. In addition, some coefficients, such as the albedos (A_1 and A_2) and the gravity-darkening coefficients (g_1 and g_2), were taken from the tables given by Lucy (1967); Ruciński (1969); van Hamme (1993), considering the possible temperatures of both components. The rest of the parameters, such as the dimensionless potentials (Ω_1 and Ω_2), the fractional luminosity (L_1) of the primary component, the inclination (i) and the mass ratio (q) of the system, were taken as the adjustable free parameters in the analysis process. The initial attempt clearly indicates the detached configuration, which corresponds to Mod2 in the Wilson Devinney code, thus we adopt detached configuration during modelling process. This configuration provides astrophysically acceptable solutions. All the parameters obtained from the light curve analysis are listed as the Solution 1 in Table 3, while the synthetic light curve obtained with these parameters are shown in the left panel of Fig. 5.

In this analysis continued under these assumption, we found a very large third light excess. About $\sim 70\%$ of all total light seems to be come from a possible third body. Here it should also be noted that the errors of temperatures were found to be between 1 K and 10 K due to the statistical calculations. However, these values do not seem to be real situation. Because of this, we assumed that the secondary component temperature error is 200 K considering mass ratio.

In the case of both Solution 1 and Solution 2, the obtained temperatures are nearly the same for both components. Using the calibrations given by Cox (2000), we tried to estimate the masses of the components depending on their temperatures. The masses of the components were found to be $0.36 M_\odot$ and $0.74 M_\odot$, respectively. Following the Kepler's third law, in the second step, using fractional radii listed in Table 3, we estimated the radii of the primary and secondary components as $0.98 R_\odot$ and $8.90 R_\odot$. Depending on these parameters, KIC 4473933's components are plotted in the Hertzsprung Russell diagram in Fig. 6 to see their evolutionary status. All absolute parameters are tabulated in Table 4.

Considering that the primary component is a main-

Table 3. The parameters obtained from the light curve analyses of the eclipsing binary system.

Parameter	Solution 1	Solution 2	Solution 3
q	1.75 ± 0.05	2.11 ± 0.08	7.32 ± 0.15
i ($^\circ$)	89.63 ± 0.03	86.20 ± 0.40	83.99 ± 0.41
T_1 (K)	4575 (fixed)	4454 ± 220	7061 ± 250
T_2 (K)	3522 ± 200	3547 ± 210	4532 (fixed)
Ω_1	55.61 ± 0.09	100.53 ± 0.11	78.86 ± 0.80
Ω_2	19.64 ± 0.01	23.04 ± 0.02	53.17 ± 0.04
L_1/L_T	0.0779 ± 0.0001	0.0776 ± 0.0001	0.8940 ± 0.0001
L_2/L_T	0.2139 ± 0.0001	0.9224 ± 0.0002	0.1060 ± 0.0001
L_3/L_T	0.7082 ± 0.0011	-	-
LDL*	linear, linear	logarithmic, logarithmic	logarithmic, logarithmic
x_1, x_2	0.712, 0.815	-0.264, 0.225	0.000, 0.000
g_1, g_2	0.32, 0.32 (fixed)	1, 0.02 (fixed)	0.32, 0.32 (fixed)
A_1, A_2	0.50, 0.50 (fixed)	0.50, 0.50 (fixed)	0.50, 0.50 (fixed)
e	0.24775 ± 0.00008	0.24816 ± 0.00008	0.24816 ± 0.00008
ω ($^\circ$)	7.27 ± 0.13	6.45 ± 0.17	6.40 ± 0.15
$\langle r_1 \rangle$	0.01874 ± 0.00003	0.01031 ± 0.00002	0.01446 ± 0.00021
$\langle r_2 \rangle$	0.09367 ± 0.00006	0.09440 ± 0.00004	0.13324 ± 0.00243
rms	0.00014	0.00015	0.00023

* LDL: Limb Darkening Law

Table 4. The absolute parameters of the components.

Parameter	Primary Component	Secondary Component
Mass (M_\odot)	0.36	0.74
Radius (R_\odot)	0.98	8.90
Temperature (K)	~ 4575	~ 3522
m_{bol} (mag)	5.80	2.14
$\log g$ (cgs)	4.01	2.41
L (erg/sec)	1.45×10^{33}	4.19×10^{34}
L (L_\odot)	0.378	10.935

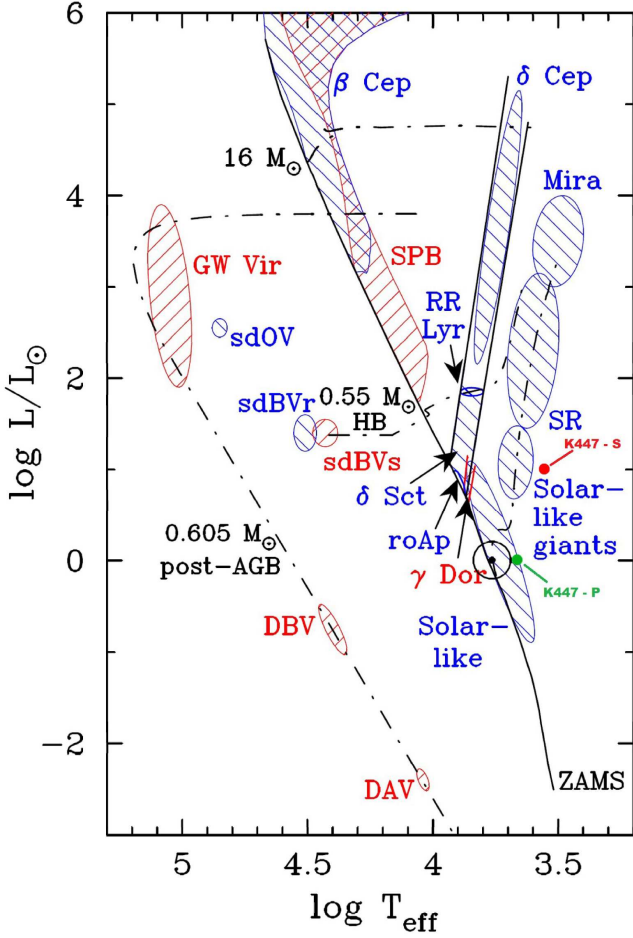


Figure 6. The locations of KIC 4473933's components in the Hertzsprung Russell diagram. We plot the primary (by the green dot, K447-P) and the secondary (by the red dot, K447-S) components of KIC4473933 on the diagram taken from the right panel of Fig. 1 given by [Handler \(2013\)](#).

sequence star, whose mass and radius were estimated, using the calibrations given by [Cox \(2000\)](#), based on the temperature obtained from Solution 1. However, since the secondary component seems to be an evolved as a giant star. Because of this, its mass and radius parameters could not be estimated. This is because the calibration table does not include any information about the temperatures in the case of these evolved stars. However, considering both the temperature and the log-g values found from the spectrum, we can just foresee that the secondary component's mass should be at least $1.2 M_{\odot}$ and its radius should be higher than $25 R_{\odot}$ according to the calibration table.

In the second place, we assumed that there could not be any third light excess about $\sim 70\%$ in the total light. Then, we assumed that there should be no third light excess in the total light. In this second way, we took the temperatures of both components as adjustable parameter. The parameters, such as the dimensionless potentials (Ω_1 and Ω_2), the fractional luminosity (L_1) of the primary component and the mass ratio (q) of the system, were taken as the adjustable free parameters in the analysis process. The initial attempt indicates no acceptable solution. Considering the deformation in the minima, the

Table 5. Frequency list of observed by the ground-based telescopes of ASAS [Bernhard & Frank \(2006\)](#).

Freq. No	Frequency	Amplitude	Phase
F1	0.0147982	0.1279081	0.7978668
F2	0.0151169	0.0498904	0.4953946
F3	0.0137188	0.0326610	0.0912521
F4	0.0329491	0.0277546	0.3945262
F5	0.0259313	0.0240060	0.4754809
F6	0.0558471	0.0237287	0.3069433
F7	0.0816906	0.0224575	0.6427021
F8	0.0466879	0.0207619	0.1234908
F9	0.0258868	0.0198807	0.3897843
F10	0.1043700	0.0195663	0.6096110
F11	0.1652342	0.0192231	0.4927472
F12	0.1537944	0.0183324	0.6676928
F13	0.0398273	0.0161801	0.6614385
F14	0.0542026	0.0154721	0.9749279
F15	0.1015405	0.0136140	0.5228277

gravity-darkening coefficients (g_1, g_2) and the limb-darkening coefficients were also taken as an adjustable free parameters. Interestingly, we obtained an other solution with out any third light excess. The obtained parameters in this analysis are tabulated as the Solution 2 in Table 3, while obtained the synthetic light curve is plotted in the middle panel of Fig. 5. In this analysis, the temperatures and fractional radii are nearly as same as the parameters obtained in the previous analysis. For this reason, the absolute parameters of the components are also identical to those of the previous analysis.

In the last place, we were tried a new analysis under a little complex assumption, in which there is no third light excess and also the temperature of T_2 is taken as fixed to 4532 K, while the temperature of T_1 is taken as a adjustable free parameter. The obtained new model is shown in the right panel of Fig. 5, while the parameters are tabulated in the last column of Table 3. The synthetic light curve is almost consistent with the observations.

2.4 Target's Problematic Nature

The light curve analysis of KIC 4473933's Kepler observations has revealed the presence of a problem. A very large third light excess was found to be as much as $\sim 70\%$ in its total light. It means that target's all brightnesses given in the literature are mainly coming from the third body. In this case, the temperatures given in the literature must be so dominantly effected by the third body. Therefore, KIC 4473933's temperatures we used in the light curve analysis seem to belong to neither the primary nor the secondary components. Because of this, we took a spectrum for the target. Indeed, we noticed that the spectrum is not be modeled by the parameters found by the light curve analysis, neither by each component nor by their combination. As it can be seen in Fig. 2, according to the spectroscopy, one of the light sources should also be the third body. We only see spectrum of a single star, not the spectrum of an eclipsing binary. Using a spectrograph with higher resolution, it might be possible to detect spectral lines of the components of the eclipsing binary KIC 4473933.

Looking at the locations of the components in the Hertzsprung Russell diagram shown in Fig. 6 are considered, it is noticeable that the primary component is located so close

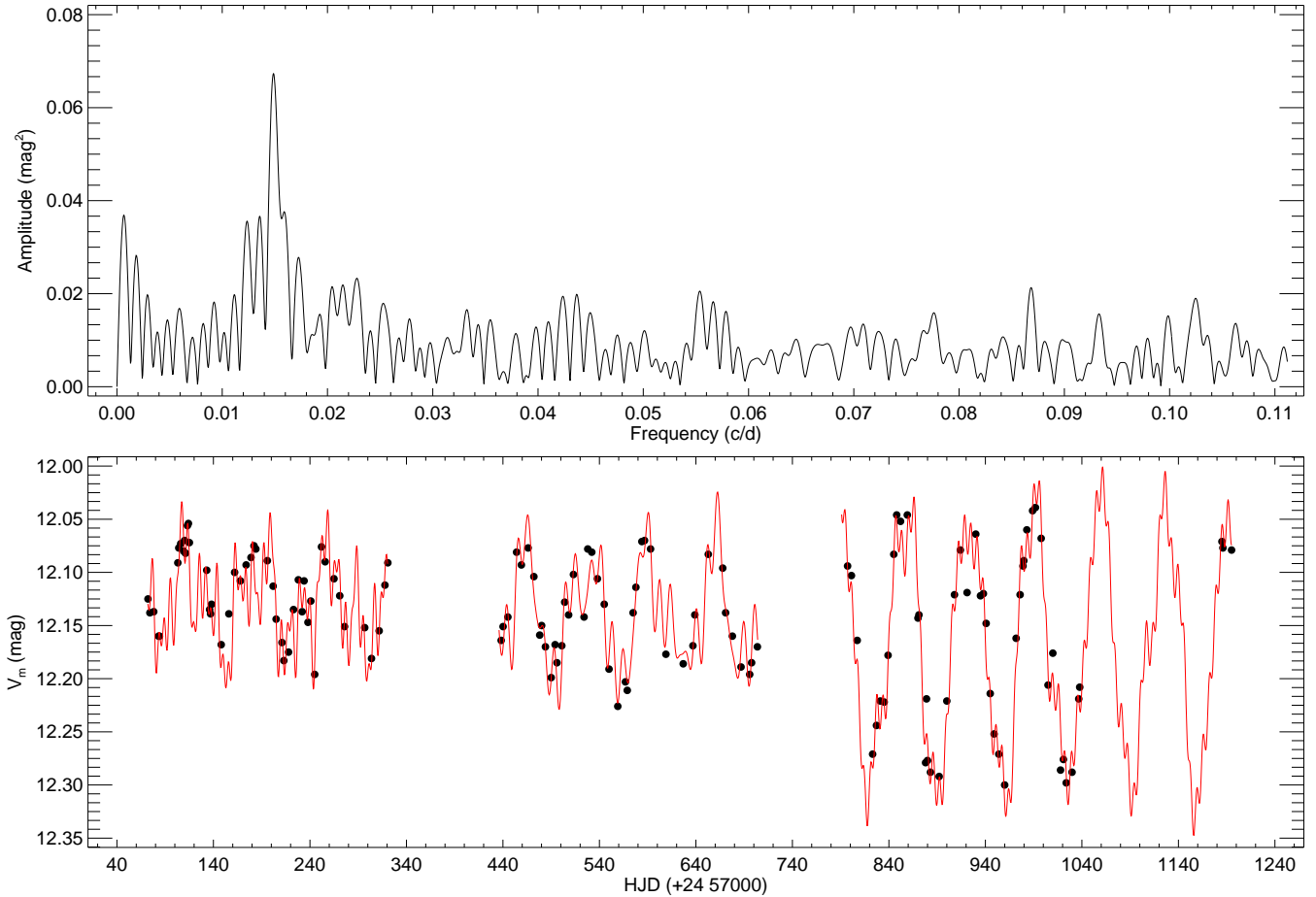


Figure 7. KIC 4473933's variation observed by the ground-based telescopes of ASAS (Bernhard & Frank 2006) with the synthetic model is shown in the bottom panel, while the frequencies obtained from the DFT are shown in the upper panel. In the bottom panel, the filled circles represent the observations, while the red line represents the model.

to the main sequence branch, while the secondary component is located on the RGB branch. Considering these locations, the primary component could be a candidate for a Solar like pulsating star, while the secondary component can be just a chromospherically active target. In this aim, we analysed the residual data obtained by extracting the synthetic curve from the Kepler observations. The residual data were analyzed to be found any pulsation frequencies, using the PERIOD04 software (Lenz & Breger 2005) that is based on the Discrete Fourier Transform (hereafter DFT) method (Scargle 1982). The analyses indicated that the residuals seem to have a random oscillation due to the granulation motions on the stellar surface or a technical noise of the observation system. On the other hand, we also took another photometric observations obtained by the ground-based telescopes of the All Sky Automated Survey (hereafter ASAS) (Bernhard & Frank 2006). A remarkable variation with a variable amplitude is seen in the ground-based data, then we analyzed the data in the same way. We found a dominant frequency of 0.014798 d^{-1} with its alias frequencies tabulated in Table 5. The Fourier amplitude spectrum derived from the DFT analysis is plotted in the upper panel of Fig. 7, while the derived model is plotted together with the ASAS light curve in the bottom panel of Fig. 7.

In this result, the target seem to show a variation with the

period of 67.575786 d. This period is so close to the period mentioned as the rotation period of the target by Benbakoura et al. (2021) depending on the target's single line spectrum. They give the rotation period of the target as $68.4 \pm 6.1 \text{ d}$. If the period we found is a rotational period as mentioned by Benbakoura et al. (2021), it must be caused by a rotational modulation effect. Then, it is expected that the ASAS data should exhibit a cyclic sinusoidal variation. To check this expectation, we phased the ASAS data by using the period of 67.575786 d we found. As it is seen from Fig. 8, indeed the data really show a cyclic sinusoidal variation, which shape and amplitude are dramatically vary by time. Considering the time of shape and amplitude variations, we separated the ASAS data into six subset data. We show the sinusoidal variations obtained from these subset data in Fig. 8. Then, we determined the averaged brightness (V_{mean}) of the sinusoidal variation as well as its amplitude for each subset. Then, we determined the rotational period (P_{rot}) of each subset data by using the PERIOD04 software (Lenz & Breger 2005). All these parameters are tabulated in Table 6. The variations of V_{mean} , amplitude and P_{rot} are plotted in Fig. 8.

In the next step, we separately modelled the variation of each subset by Fourier method, assuming that there could be several spotted areas on the active component. The Fourier

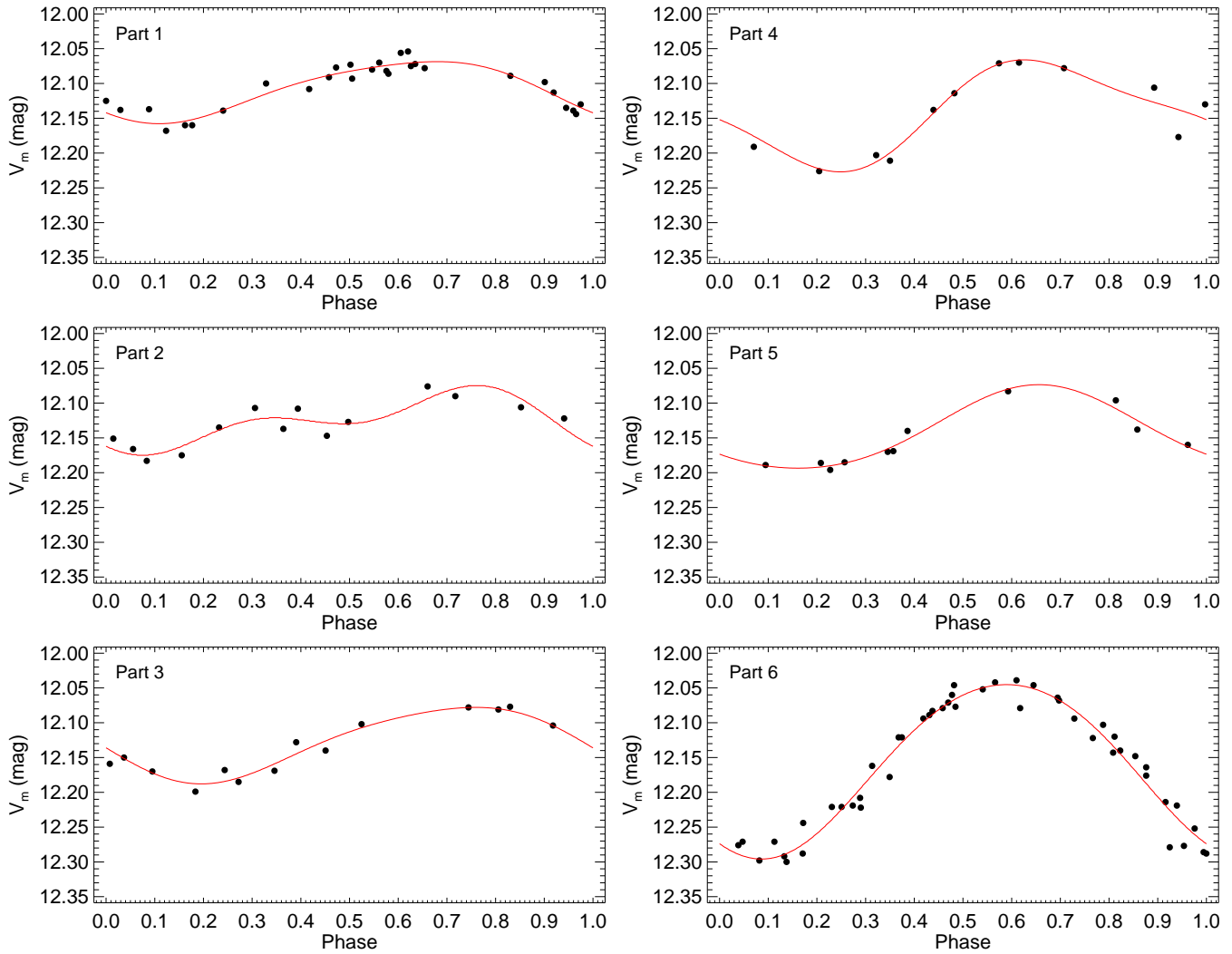


Figure 8. Each cycle of the sinusoidal variations obtained from the ASAS data is shown. The filled circles represent the observations, while the red line represents the model.

Table 6. The parameters determined from the sinusoidal variations of ASAS subset data are listed.

Subset	HJD	V_{mean} (mag)	Amplitude (mag)	P_{rot} (d)
1	2457133.69168	12.113	0.089	66.40711
2	2457239.78751	12.125	0.100	81.04294
2	2457239.78751	12.148	0.054	81.04294
3	2457496.19856	12.133	0.110	65.94809
4	2457571.08909	12.147	0.161	52.55802
5	2457668.68864	12.133	0.120	66.87923
6	2457937.55703	12.170	0.250	67.36251

models of the sinusoidal variations are shown by the red line in Fig. 8. As it is seen from the figure, the analyses demonstrated that there are just two dominant spotted areas on the surface. Finally, we computed the minima phases of the sinusoidal variation seen in each subset data. Assuming the first subset data as the first cycle, we added the number of cycles required by considering their observation time to each minima phases. Thus,

we obtained theta min (θ_{min}) variation. Using the least squares method, we modelled θ_{min} variations with the linear function. We plotted the sinusoidal minima phases and θ_{min} variations versus the time for both spotted areas. Regression calculations of the linear model of the θ_{min} variations indicated that the longitudinal migration periods are 87.719 d for the first spotted area and 94.340 d for the second spotted area on the surface.

3 Results and Discussion

There are rarely studies in the literature about the target, though there are several points waiting to solve. For example, KIC 4473933 is debated as a target having a terrestrial planet by [Burke et al. \(2015\)](#), while KIC 4473933 could be a rapidly rotating giant star, according to [Costa et al. \(2015\)](#). On the other hand, KIC 4473933 is classified as an eclipsing binary system in the SIMBAD Database, and we have found that the target an eclipsing binary, too.

In the analysis, we can get an astrophysically acceptable solution for the target, using the PyWD2015 software ([Güzel & Özdarcın 2020](#)). In the case of the Solution 1 and Solution 2, we find that the secondary component is possibly evolved star

from the main sequence, and now it must be a giant or sub-giant star. According to the results, we have tried to estimate stellar parameters. Considering its found temperature, the primary component's mass was computed as $0.36 M_{\odot}$, while its radius was found to be $0.98 R_{\odot}$. For the secondary component, the mass was found to be $0.74 M_{\odot}$, while its radius was found to be $8.90 R_{\odot}$. Here are two points to be noted. First of all, the mass ratios found from the solutions are a bit different from the mass ratio found by the computed absolute parameters. This is because the calibrations used by the PyWD2015 software are different from the calibrations given by Cox (2000). Secondly, we particularly note that there is a very large third light excess ($\sim 70\%$) in the total light, which highly reduces accuracy of physical parameters of the components. Because of this, the ratio of the light coming from both the primary and the secondary components is $\sim 30\%$. According to the Solution 1, the third body should be so dominant source in the system that one expects to see its effect on the $(O-C)_{II}$ residuals, which does not exhibit any sinusoidal variation. There should be two reasons for the case. Firstly, possible third body could not be a member of the system. Secondly, third body is the member of the system, but the observing time interval as long as a few years is not enough to see any sinusoidal variation in the $(O-C)_{II}$ residuals.

In the case of the Solution 1, the third light excess seems to be ($\sim 70\%$) in the total light. However, we do not see any indicator in the spectrum for the third component. Because of this, we also tried to analyse the light curve in the second and third ways under some different assumptions. As it is seen from Table 3, we obtained a second solution with the unstable gravity-darkening and limb-darkening coefficients. Considering the deformation in the minima, we took all of them as an adjustable free parameters. We obtained nearly the same parameters for both Solution 1 and 2. However, in the case of the Solution 2, the secondary component's luminosity is increased in order to compensate the luminosity excess due to the third body by decreasing the primary component's temperature and fractional radius. We tried another analysis under a little complex assumption as mentioned in §2.3. Although the synthetic light curve obtained by the Solution 3 is compatible with the observations, the obtained temperature of T_1 does not match the temperature obtained from the spectrum. When we consider the difference between the components' luminosities, we expect to find that the temperature of the primary component is dominant. As it is as same as the previous case, in the case of the Solution 3, the primary component's temperature is increased in order to compensate the luminosity excess due to the third body found in the Solution 1. Meanwhile, the fractional radii are also a bit varied to ensure the Solution 3. If this case was valid, we would obtain the primary component's temperature about 7061 K from the spectrum. However, the highest temperature obtained from the spectrum is 4500 K. Considering the obtained temperatures, radii and luminosities in the Solution 3, the results are not in agreement with the results found from the spectrum. The difference between the luminosities of the components is about 9 times. Therefore, the temperature obtained from the spectrum should belong to the component with the highest luminosity. However, the temperature obtained from the spectrum (4500 K) and the temperature obtained from the light curve analysis (7061 K) are quite different from each other. Although the synthetic light curve is

model the observations very well, the results are not astrophysically acceptable.

The $(O-C)_{II}$ residuals do not exhibit any variation, the residuals of both minima are also intertwined among themselves. But, we expect a separation between the $(O-C)_{II}$ residuals of the primary and secondary minima in the case of an eclipsing binary system. As it is seen from Fig. 4, the minima times caused the transits exhibits a regular linear variation with the scattering is about in range of 1 day. Because of the insufficient data, it is very hard to discuss the phenomenon, but it should be followed in the future.

For the target, we examined the variations seen at out-of-eclipses in the light curve and we detected some sinusoidal variations. When the data obtained as a result of spectral observation we obtained were examined, any direct emission or emission-like structure do not detected in the lines. This result indicates that the source of light variation at out-of-eclipses is not a chromospheric activity. However, Benbakoura et al. (2021) indicated that the system exhibits remarkably Ca II H&K emission, which is an indicator for the chromospheric activity. In this point, the frequency analyses of the residuals obtained in the light curve analysis of the Kepler data do not indicate any sinusoidal variation due to the rotational modulation. On the other hand, we found the period of 67.575786 d from the frequency analyses of the ASAS data. When we plotted the ASAS data versus the phase computed by taking the period of 67.575786 d as a rotational period, we found a systematic sinusoidal variation in the ASAS data.

Analysing the sinusoidal variation seen in each subset data, we obtained variations of the averaged brightness (V_{mean}) as well as its amplitude and the rotational period (P_{rot}) for the sinusoidal variation. As it is seen from Fig. 9, the averaged brightness of the target is decreasing, while the amplitude of the variations is rising. These results indicate that the effectiveness of the spotted areas on the active component is increasing, while they are getting closer each other around "a common location". Moreover, As it is seen from the bottom panel of Fig. 9, the rotational periods determined from each subset data are slightly decreasing time by time. It means that the location the spotted areas getting around is slightly migrating toward the stellar equator, where the rotational velocity is the highest under an assumption of the classical differential rotation.

In Fig. 10, the θ_{min} variations are seen. When we modelled the θ_{min} migrations with the linear functions, we found that the migration periods of the spotted areas on the stellar surface are found to be 87.719 d for the first spotted area and 94.340 d for the second spotted area. It means that the spotted areas on the surface seem to slightly migrate toward the stellar equator.

Acknowledgement

We thank the referee for useful comments that have contributed to the improvement of the paper. We wish to thank the Turkish Scientific and Technical Research Council for supporting this work through grant No. 116F213. We thank to Ege University Observatory for a partial support in using R40. We wish to thank TÜBİTAK National Observatory for a partial support in using RTT-150 (Russian-Turkish 1.5-m telescope in Antalya) with the project number 14BRTT150-667.

References

- Benbakoura M., et al., 2021, *A&A*, 648, A113
Bernhard K., Frank P., 2006, *IBVS*, 5719, 1, [ADS](#)

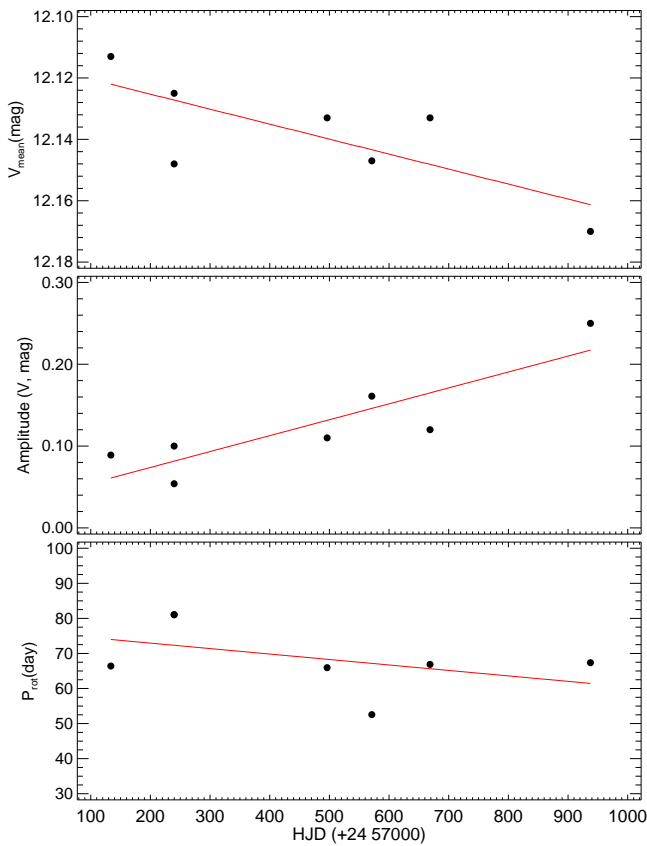


Figure 9. The variations of the V_{mean} , amplitude and rotational period (P_{rot}) determined from each cycle of the sinusoidal variations. The filled circles represent the observed parameters, while the red line represents the model.

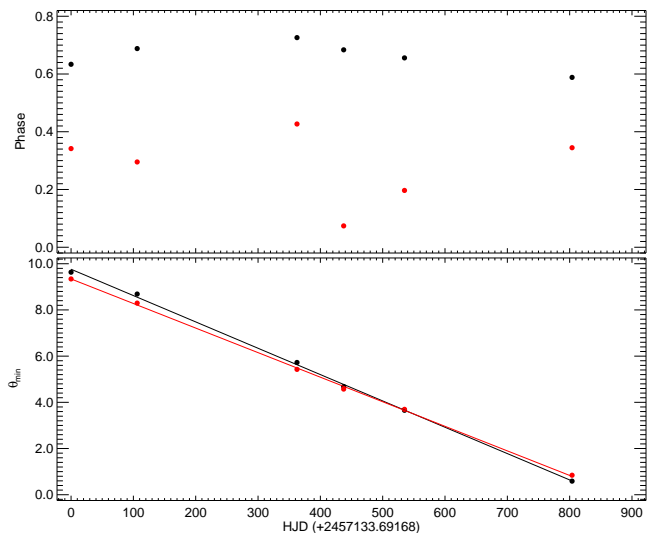


Figure 10. The θ_{min} variation obtained by determining the spot minima phases from the sinusoidal variations is shown. The filled circles represent the observed parameters, while the red line represents the model.

Blanco-Cuaresma S., Soubiran C., Heiter U., Jofré P., 2014, *A&A*, 569, A111
 Borucki W. J., et al., 2010, *Science*, 327, 977
 Burke C. J., et al., 2015, *ApJ*, 809, 8
 Caldwell D. A., et al., 2010, *ApJ*, 713, L92
 Castelli F., Kurucz R. L., 2004, ArXiv Astrophysics e-prints, , *ADS*
 Costa A. D., et al., 2015, *ApJ*, 807, L21
 Cox A. N., 2000, *Allen's astrophysical quantities*. AIP Press; Springer, New York
 Egret D., Didelon P., McLean B. J., Russell J. L., Turon C., 1992, *A&A*, 258, 217, *ADS*
 Frasca A., Covino E., Spezzi L., Alcalá J. M., Marilli E., Fžrész G., Gandolfi D., 2009, *A&A*, 508, 1313
 Gray R. O., Corbally C. J., 1994, *AJ*, 107, 742
 Gray R. O., Napier M. G., Winkler L. I., 2001, *AJ*, 121, 2148
 Gray R. O., Corbally C. J., Garrison R. F., McFadden M. T., Robinson P. E., 2003, *AJ*, 126, 2048
 Gray R. O., Corbally C. J., Garrison R. F., McFadden M. T., Bubar E. J., McGahee C. E., O'Donoghue A. A., Knox E. R., 2006, *AJ*, 132, 161
 Güzel O., Özdarcan O., 2020, *Contributions of the Astronomical Observatory Skalnaté Pleso*, 50, 535
 Handler G., 2013, *Asteroseismology*. Springer Netherlands, Dordrecht, p. 207, doi:10.1007/978-94-007-5615-1_4
 Hardie R. H., 1964, *Photoelectric Reductions*. the University of Chicago Press, p. 178
 Henden A. A., Levine S., Terrell D., Welch D. L., 2015, in *AAS Meeting Abstracts #225*. p. 336.16
 Jenkins J. M., et al., 2010a, *ApJ*, 713, L87
 Jenkins J. M., et al., 2010b, in *Software and Cyberinfrastructure for Astronomy*. p. 77400D, doi:10.1117/12.856764
 Kirk B., et al., 2016, *AJ*, 151, 68
 Koch D. G., et al., 2010, *ApJ*, 713, L79
 Kron G. E., 1952, *ApJ*, 115, 301
 Kunkel W. E., 1975, in *Sherwood V. E., Plaut L., eds, Variable Stars and Stellar Evolution Vol. 67, Variable Stars and Stellar Evolution*. p. 15
 Kwee K. K., van Woerden H., 1956, *Bull. Astron. Inst. Netherlands*, 12, 327, *ADS*
 Lenz P., Breger M., 2005, *Communications in Asteroseismology*, 146, 53
 López-Morales M., 2007, *ApJ*, 660, 732
 Lucy L. B., 1967, *Z. Astrophys.*, 65, 89, *ADS*
 Mathur S., et al., 2017, *ApJS*, 229, 30
 Matijevič G., Prša A., Orosz J. A., Welsh W. F., Bloemen S., Barclay T., 2012, *AJ*, 143, 123
 Morales J. C., Ribas I., Jordi C., 2008, *A&A*, 478, 507
 Morales J. C., Gallardo J., Ribas I., Jordi C., Baraffe I., Chabrier G., 2010, *ApJ*, 718, 502
 Rodono M., 1986, *The atmospheres of M dwarfs: Observations*. NASA, Washington, pp 409–453
 Ruciński S. M., 1969, *Acta Astronomica*, 19, 245, *ADS*
 Ryabchikova T., Piskunov N., Kurucz R. L., Stempels H. C., Heiter U., Pakhomov Y., Barklem P. S., 2015, *Phys. Scr.*, 90, 054005
 Scargle J. D., 1982, *ApJ*, 263, 835
 Slawson R. W., et al., 2011, *AJ*, 142, 160
 Tayar J., et al., 2015, *ApJ*, 807, 82
 Thomas J. H., Weiss N. O., 2008, *Sunspots and Starspots*. Cambridge University Press, Cambridge, UK
 Tonry J., Davis M., 1979, *AJ*, 84, 1511
 Wilson R. E., Devinney E. J., 1971, *ApJ*, 166, 605
 Wilson R. E., Van Hamme W., 2014, *ApJ*, 780, 151
 Zacharias N., Monet D. G., Levine S. E., Urban S. E., Gaume R., Wycoff G. L., 2004, in *AAS Meeting Abstracts*. p. 1418
 van Hamme W., 1993, *AJ*, 106, 2096

Access:

M21-0201: *Turkish J.A&A* — Vol.2, Issue 2.